Catalysis Today 141 (2009) 144–151

Contents lists available at ScienceDirect

Catalysis Today

journal homepage: www.elsevier.com/locate/cattod

Photocatalytic mineralization of benzene over gold containing titania nanotubes: Role of adsorbed water and nanosize gold crystallites

S.V. Awate, R.K. Sahu, M.D. Kadgaonkar, R. Kumar, N.M. Gupta *

Catalysis Division, National Chemical Laboratory, Dr. Homi Bhabha Road, Pune 411008, India

ARTICLE INFO

Article history:
Available online 27 May 2008

Keywords:
TiO_2 nanotubes
Gold containing
Photocatalyst
Benzene degradation
Role of adsorbed water
Transient species

ABSTRACT

Well aligned titania nanotubes, with surface area of ~150 $m^2 g^{-1}$ and average pore diameter of ~5 nm, have been synthesized by subjecting a mesoporous TiO_2 sample to alkaline treatment followed by calcination at different temperatures. Composite catalysts with gold particles dispersed in these nanotubes were also synthesized and their structural, morphological, optical and photocatalytic properties were examined. The catalytic activity of TiO_2 for UV-mediated photo-oxidation of benzene was found to be affected by several factors, such as the sample texture, presence of adsorbed water and gold crystallites. The overall conversion of benzene to form CO_2 followed a trend: Au/nanotube > TiO_2 nanotubes > mesoporous TiO_2. *In situ* IR spectroscopy revealed that the adsorption and reaction of benzene molecules gave rise to formation of certain phenolic species over TiO_2, while the temperature-programmed desorption (TPD) study showed that the Au/TiO_2 interfaces serve as distinct sites for the adsorption and activation of oxygen molecules. It is suggested that certain hydroxyl and oxygen ion radicals produced under UV-irradiation may promote the deep oxidation of surface phenolic species and phenoxyl ($ArO^{\bullet}$) type transient radicals.

1. Introduction

The photo-oxidation of benzene has been investigated earlier, both under aqueous as well as vapor phase reaction conditions. These studies were in general aimed at finding a viable route for purification of air by removal of volatile organic compounds or alternatively to develop a green chemistry route for selectively converting benzene into certain value added products such as phenols [1–13]. Various conflicting observations have, however, been reported. Thus, Fu et al. [1] found that the gas phase photo-degradation of benzene over sol–gel prepared titania gave rise to carbon dioxide and water without forming any detectable organic products and the conversion of benzene was improved on platinum dispersion. Using an aqueous suspension of TiO_2, Park and Choi [2] reported the direct conversion of benzene to phenol and dihydroxylated products such as hydroquinone and catechol, where OH radicals generated on UV illumination played an important role. Using the techniques of temperature-programmed oxidation and desorption (TPO, TPD), Larson and Falconer [3] showed that the intermediate species formed during photocatalytic oxidation of aromatics are adsorbed strongly and are less reactive, as compared to the original aromatic reactant. Einaga et al. [4] reported the production of CO_2 and CO during the gas phase decomposition of benzene over TiO_2 at room temperature along with the formation of phenol and certain polymeric products. The oxygen and water vapor present in the reacting stream are found to help in re-oxidation of Ti^{3+} to Ti^{4+} and in regeneration of surface hydroxyl groups. In a more recent study on liquid phase photo-oxidation of benzene, Shimizu et al. [5] reported the formation of dihydroxy benzenes using cation exchanged BEA zeolites, while phenol and CO_2 were the main reaction products on Degussa P-25 TiO_2. In an FTIR spectroscopy study on adsorption and reaction over powdered TiO_2, Wu et al. [8] suggested that the benzene molecules are adsorbed with their π-electrons interacting with surface Ti^{4+} ions. The benzene in this adsorbed state was found to be stable even after elevation of sample temperature to 400 °C while the reaction products H_2O, CO_2 and CO were produced at temperatures lower than 225 °C and only in the presence of oxygen. According to a kinetic study of Doucet et al. [11], the relative humidity plays no role in the primary attack of benzene molecules at titania surface while it helps in the degradation of some surface species. Various aspects of photocatalytic oxidation of benzene, such as the reaction pathways, role of titania morphology, role of a noble metal co-catalyst, and the contribution of water vapor present in reaction mixture, thus need to be understood clearly.

* Corresponding author. Tel.: +91 20 2590 2008; fax: +91 20 2590 2633.
E-mail address: nm.gupta@ncl.res.in (N.M. Gupta).

0920-5861/$ – see front matter © 2008 Elsevier B.V. All rights reserved.
doi:10.1016/j.cattod.2008.04.008

In a recent study [14], we reported that the gold nanocrystallites dispersed in mesoporousTiO_2 serve as distinct oxygen adsorption sites and give rise to enhanced photocatalytic activity for vapor phase oxidation of volatile organic compounds. Utilizing similar mesoporous TiO_2 as precursor, we have now synthesized titania samples of tubular morphology with an objective to further augment the number of adsorption sites and to facilitate the transport of reactant molecules through their porous network. The procedure described in some of the earlier studies [15–18] has been adopted for this purpose. Corresponding gold containing TiO_2 nanotubes were prepared by impregnation. The present communication deals with physico-chemical properties of Au/TiO_2 nanotubes and their photocatalytic activity for benzene oxidation. The transient species formed over TiO_2 and Au/TiO_2 surfaces after exposure to benzene + air, without and in presence of moisture, were examined with the help of *in situ* Fourier-transform infrared (FTIR) spectroscopy. Effect of gold crystallites on adsorption characteristics of different samples was also investigated by recording the temperature-programmed desorption of oxygen (TPD-O_2). The reaction pathways involved in photocatalytic oxidation of benzene and the role played by gold nanocrystallites in the process have been elucidated on the basis of these measurements.

2. Experimental

The titania nanotubes were synthesized by utilizing a mesoporous TiO_2 sample, the details of which are described earlier [14], as precursor. For the preparation of this TiO_2 about 10 ml of Ti(IV) isopropoxide (Aldrich) was added slowly to 1N HCl containing tartaric acid (3.6 g). The HCl/alkoxide ratio was ~1 and the solution was stirred constantly for a period of about 1 h. The mixture was then heated at 403 K for 24 h in a teflon-lined autoclave. After cooling and centrifugation, the mass was dried (373 K) and finally calcined at 623 K for ~3 h. This sample is denoted as T1 in the text.

For the preparation of TiO_2 nanotubes, 2 g of sample T1 was stirred with 10 M NaOH solution in a sealed polythene reactor, and was maintained at a temperature of 393 K for 3 days. HCl solution was then added drop wise until the pH was ~1.5, followed by stirring for 24 h. After centrifugation, the precipitate was washed several times with water. The mass was finally freeze-dried (230 K) for 24 h. This sample, referred to as as-synthesized nanotube (T2), was subjected to calcination for 3 h at three different temperatures, i.e. 423, 523 and 623 K, and the samples are denoted, respectively, as T3, T4 and T5 (Table 1). For incorporation of gold, a representative nanotube sample T3 was impregnated with isopropanol solution of tetrachloroauric acid. After drying, the sample was heated again in air at 423 K and contained ~1 wt% of gold (denoted as Au/T3).

The catalysts were characterized for their structural, optical and photocatalytic properties. The powder XRD patterns were recorded on a Rigaku, Miniflex (D Max III VC) XRD machine (Cu Kα radiation), operated at 30 kV and 15 mA. TEM images were obtained on a JEOL-2010 CX microscope. The information about the BET surface area and the pore characteristics of different samples was derived from the low-temperature nitrogen adsorption isotherms, recorded on a Quantachrome, NOVA 1200 equipment. Prior to recording of these data, the sample was treated at 573 K under vacuum (10^{-3} Torr) to remove the physisorbed moieties. The BJH formulation was employed to obtain the pore size distribution data. The absorbance spectra were recorded on PerkinElmer (Lambda 650) UV–vis diffuse-reflectance (DR) spectrophotometer. About 3 wt% of a sample was mixed thoroughly in barium sulphate for these measurements. In order to monitor the thermal properties, simultaneous TG/DTA plots were collected under argon atmosphere using an as-synthesized TiO_2 nanotube sample.

XPS analysis was performed on a VG Scientific ESCA-3000 spectrometer, operating at 150 W at a pressure of 10^{-9} Torr. The spectra were acquired using non-monochromatized Mg Kα radiation (1253.6 eV). The binding energy of XPS peaks was referenced to C1s line at 284.6 eV for charge compensation.

Experiments on the temperature-programmed desorption of saturation-covered oxygen were performed on a Micromeritics Autochem 2910 instrument. About 0.25 g of a fresh sample was placed in a U-shaped flow-through, quartz microreactor for each experiment. The sample was activated at 600 K for 3 h under He flow (20 ml min^{-1}) and then cooled to ambient temperature before being exposed to O_2 (~20 vol% in He) flow for 30 min. The sample was flushed again with He for about 15 min to remove physisorbed oxygen, and a desorption profile was then recorded by increasing the sample temperature to 1000 K at a ramp rate of 10 K/min.

The photocatalytic oxidation of benzene was performed under UV radiation (400 W medium-pressure mercury vapor lamp, UV output 15–20%, range 225–400 nm, peak at 365 nm). The light source was housed in a water-cooled quartz jacket to cut-off infrared radiation. 25 mg of a sample was placed in a quartz photoreactor of 100 ml capacity and the benzene vapor mixed at different mol ratios (0.7–3.0 mol%) in air was introduced in the reactor for activity measurement. The experiments were conducted at room temperature and the reaction products formed as a function of radiation exposure were analyzed periodically with the help of Shimadzu model-R-15A gas chromatograph (Porapak-Q column, TCD detector).

In situ FTIR experiments were conducted both in the diffuse-reflectance and transmittance modes. A Shimadzu SSU-8000 spectrophotometer was used for DR study, and about 10 mg catalyst powder was packed in the sample holder for this purpose. The sample was kept under air flow for several hours prior to its exposure to ~10 ml mixture of benzene vapor (10 mol%) + air and the IR spectrum was recorded after a lapse of ~5 min. For the transmittance mode experiments, a self-supporting sample wafer (~80 mg) was placed in a stainless steel cell fitted with water-

Table 1
Textural properties of titania samples as a function of calcination temperature

Serial no.	Sample notation	Calcination temperature (K)	BET surface area (m^2/g)	Total pore volume (cm^3/g)	Average pore diameter (nm)	Crystallite size[#] (nm)
1	T1[a]	–	92.0	–	4.0	14.0
2	T2	As-synthesized	193.1	0.26	5.4	6.3
3	T3	423	176.5	0.24	5.5	6.3
4	T4	523	148.6	0.19	5.0	8.1
5	T5	623	77.5	0.17	–	10.0

T2–T5, titania nanotubes calcined at different temperatures.
[a] Precursor mesoporous TiO_2 sample.
[#] From XRD data using Sherrer's equation.

cooled CaF_2 windows [19]. The cell, equipped for *in situ* heat treatment under vacuum, was mounted on a Thermo Nicole (model–Nexus 870) spectrometer. The sample was activated at 600 K under vacuum for several hours, followed by cooling to room temperature and exposure to benzene (10 mol%) + air at the cell pressure of ~100 Torr. Normally 200 scans were averaged out for each plot at a resolution of 4 cm^{-1}. The sample spectrum recorded prior to benzene adsorption was compensated for plotting of the IR bands arising exclusively due to surface adsorbed species.

3. Results and discussion

The textural properties of samples T1–T5, as derived from N_2-adsorption results, are listed in Table 1. As-synthesized nanotube samples were of smaller crystallite size and accordingly higher surface area, as compared to sample T1. As shown in Table 1, the surface area decreased progressively on calcination at higher temperatures. Curves (a–d) in Fig. 1 exhibit the powder XRD profiles of TiO_2 nanotube samples calcined at different temperatures. Curve (e) shows the comparative XRD pattern of a commercial TiO_2 sample (E. Merck, India). The as-synthesized sample (T2) shows prominent XRD reflections at 2θ values of ca. 25.1°, 37.9°, 48° and 53.9°, representing (1 0 1), (0 0 4), (2 0 0) and (1 0 5) lattice planes of anatase TiO_2 (curve (a)). We also observe a weak reflection at $2\theta = 27.3°$ due to (1 1 0) plane of rutile phase, indicating its presence in a small concentration (curve (a)). The width of the XRD lines decreased with increase in calcination temperature (Fig. 1b–d). The broadening observed in these XRD lines in comparison to Fig. 1e is a characteristic feature of small (nano) size particles. The average size of crystallites in different samples, as estimated by using Scherrer's equation for $I_{1\,0\,0}$ reflection at 25.1°, is listed in Table 1. Calcination at a higher temperature of 623 K resulted in the complete removal of rutile phase (curves (d)).

All the samples exhibited a mesoporous character, as indicated by the representative N_2-adsorption/desorption isotherms in Fig. 2. The surface area of the samples decreased progressively on calcination at elevated temperatures (Table 1). The effect of calcination on pore size distribution is shown in Fig. 3. These results reveal the presence of at least two kinds of mesopores in the low-temperature calcined samples, majority being of 40–42 nm size and a smaller number having a diameter in range 50–100 nm (Fig. 3a and b). Calcination at 523 K resulted in a marginal increase of larger size pores (Fig. 3b). A wide range pore size distribution was however observed for further increase in calcination temperature to 623 K (curve (c)), which may be ascribed to unfolding of titania layers as a result of the release of trapped moisture or template molecules.

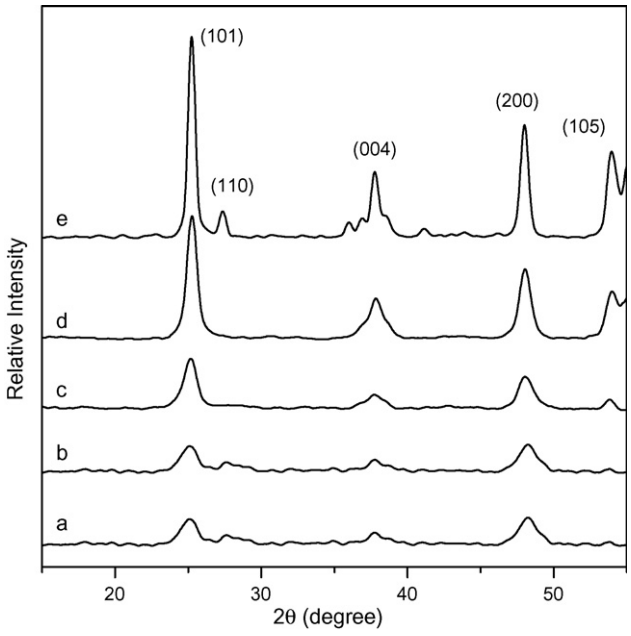

Fig. 1. XRD profiles of nanotubes prepared from mesoporous TiO_2 and calcined at different temperatures: (a) as-synthesized (T2), (b) 423 K (T3), (c) 523 K (T4) and (d) 623 K (T5). Curve (e) shows XRD pattern of a commercial TiO_2 sample (E. Merck) for comparison.

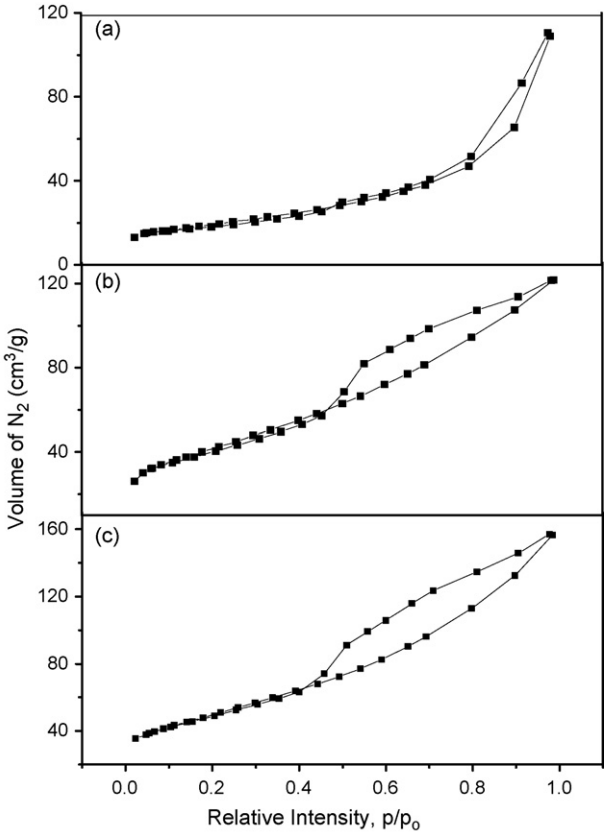

Fig. 2. Low-temperature nitrogen adsorption isotherms of titania nanotubes calcined at different temperatures. (a) T3, (b) T4, (c) T5. Sample notations as described in Table 1.

3.1. TEM results

Fig. 4A shows the representative TEM picture of sample T3. The length, the outer diameter and the inner diameter of the multi-wall nanotubes seen in this figure are estimated to be in the ranges of 60–300, 9–14 and 4–7 nm, respectively. In most of the cases the tubes appear to be in random orientations and are open at both the ends. The TEM pictures of the gold containing samples indicated the size of gold particles to be around 10–20 nm, as seen in a representative micrograph in Fig. 4B for sample Au/T3. The TEM images of sample T4 revealed marginally greater outer diameter and wider tube openings. No clear pictures could however be obtained for sample T5.

3.2. XPS analysis

Au4f XPS spectrum of Au/T3 sample exhibited peaks at the binding energy (B.E.) values of 84.3 and 87.9 eV for $4f_{7/2}$ and $4f_{5/2}$ electrons (not shown). These XPS spectra matched well, both in B.E.

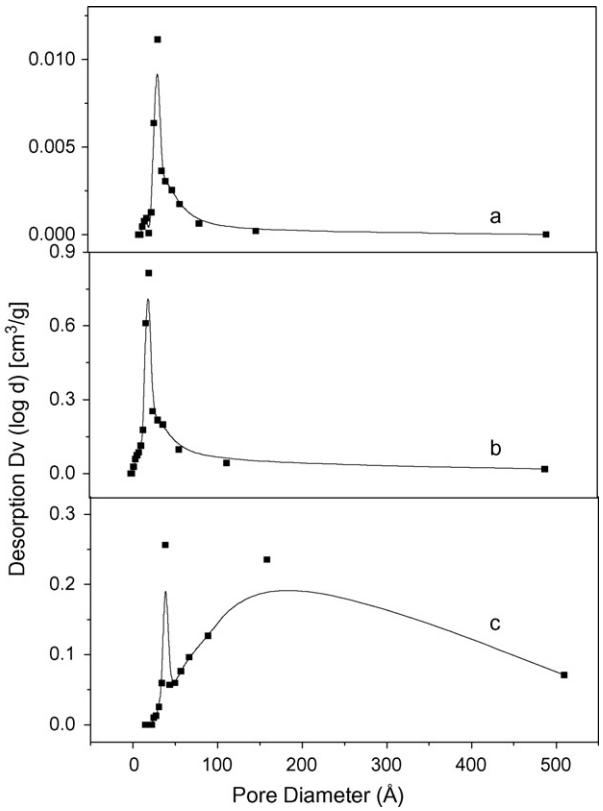

Fig. 3. Pore size distribution curves of titania nanotubes calcined at different temperatures: (a) T3, (b) T4 and (c) T5. Sample notations as described in Table 1.

and peak width, with the corresponding data recorded for a pure gold powder sample and also with the XPS data reported for small gold particles [20]. Similarly, the Ti $2p_{1/2}$ and $2p_{3/2}$ signals were observed at B.E. values of 464.6 and 458.9 eV for gold-free titania (sample T1), which correspond well with the values reported for mesostructured TiO_2 [21].

Overall, the XPS results matched with the mesoporous nature of our titania samples and confirmed the zero valent state of deposited gold.

3.3. Thermal analysis

Fig. 5 exhibits differential thermal analysis (DTA) and differential thermal gravimetry (DTG) curves, recorded on as-synthesized titania nanotube sample (T2). An endotherm peaking at ~400 K corresponds to a major weight loss in temperature range 300–475 K and can be correlated with the release of adsorbed water. At higher temperatures, we see small step-wise weight loss, with the associated high endothermicity. Since the substrate was free of any other contamination, we attribute these observations to the collapse of nanotube structure on removal of water or trapped tartaric acid molecules. These observations are in agreement with the pore size distribution data of Fig. 3c.

3.4. Optical absorption properties

Curves (b) and (c) in Fig. 6 present the diffuse-reflectance UV–vis spectra of representative samples T3 and Au/T3, respectively. Curve (a) shows comparative spectrum of precursor TiO_2 sample T1. As compared to titania nanotubes (T3), the absorbance in UV region is found to increase considerably on gold dispersion (curve (c)). In addition to the changes in the intensity of absorbance

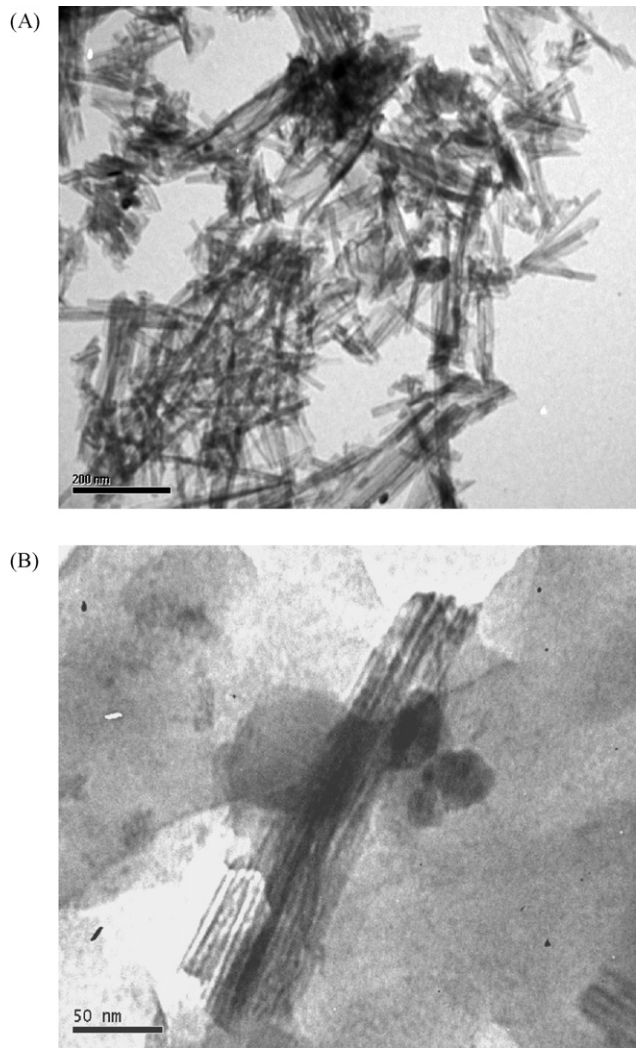

Fig. 4. TEM images of samples (A) T3 and (B) Au/T3.

spectrum, a shift to lower wavelength is also noticeable in spectra (b) and (c) of Fig. 6. We also observe a marked increase in the visible region absorbance in the case of gold-doped sample. The broad absorbance band in 500–700 nm region in curve (c) corresponds to the well-reported plasmon resonance associated with nano-structured gold particles.

3.5. Photocatalytic activity

Fig. 7 displays the batch mode photocatalytic activity of representative samples T3 and Au/T3 for oxidation of benzene (0.7–3.0 mol% in air) under ultraviolet-irradiation, where CO_2 and water were the main reaction products. The precursor TiO_2 sample T1 showed only negligible activity even after about 5 h of irradiation time (curve (a)). A conversion to the extent of about 10% benzene to CO_2 was, however, observed when some water (~100 μmol) was introduced in the reaction cell. These results are presented in curve (a) of Fig. 7. Higher conversion of benzene was observed for the gold-containing samples, both under dry and moist conditions. Also, the conversion was higher for the reaction mixtures containing lower benzene concentration in air. Curves (b–d) in Fig. 7 show the typical CO_2 yields when benzene mixed in air at different molar concentrations was reacted over Au/T3 in the presence of UV radiation. As in the case of data in curve (a), addition of water in the reaction mixture gave rise to much higher

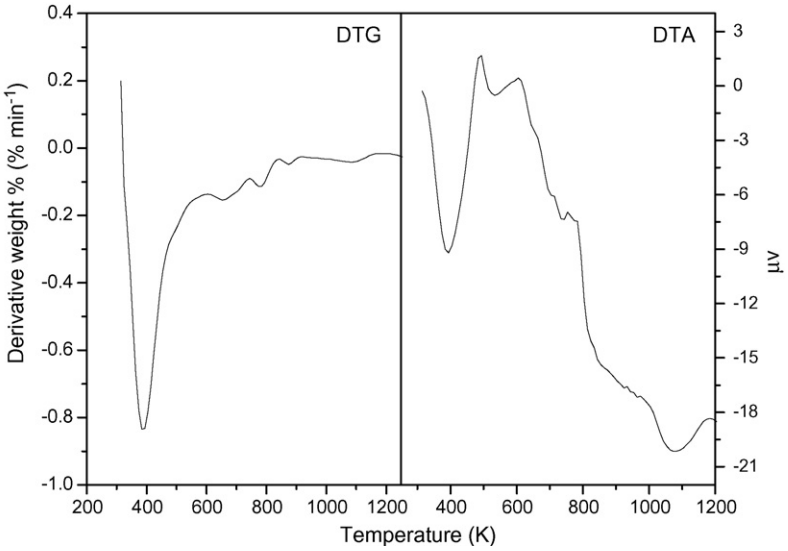

Fig. 5. DTA and DTG plots of un-calcined titania nanotubes (sample T2).

yields of CO_2 in the experiments over Au/T3 as well. The typical effect of water addition on the photocatalytic activity of Au/T3 is shown in Fig. 7e.

3.6. Temperature-programmed desorption of surface adsorbed oxygen

Fig. 8 exhibits the TPD-O_2 profiles of some representative titania samples. The non-porous E. Merck TiO_2 sample showed very weak adsorption of oxygen, as seen in a broad peak at ~460 K in curve (a) of this figure. On the other hand, an intense O_2-desorption band at a temperature maximum (*T*m) of ~760 K and a weak shoulder peak at 620 K were observed in the case of mesoporous sample T1 (Fig. 8, curve (b)). Considering the energy requirement for desorption from different possible sites of TiO_2, the 620 K band may be attributed to O_2 held at the external surface and 760 K band to the molecules occluded in the mesopores. The nanotube sample T3 at the same time showed an additional high temperature desorption peak at 870 K (curve (c)), which may be ascribed to the O_2 molecules trapped in narrow tubular structures of this sample. Furthermore, the presence of gold resulted in considerable decrease in the intensity of 760 K band and at the same time a new desorption band was observed at ~550 K, instead of a shoulder band in curves (b) and (c). A typical TPD-O_2 profile of sample Au/T3 is shown in Fig. 8d. This new desorption band at 550 K can be identified with the adsorption of O_2 at Au-TiO_2 interfacial sites. The decreased intensity of the higher temperature peaks in Fig. 8d may be ascribed to the blockage of some mesopores/tubular structures in sample T3 because of the occluded gold crystallites. This is in agreement with our N_2-adsorption results.

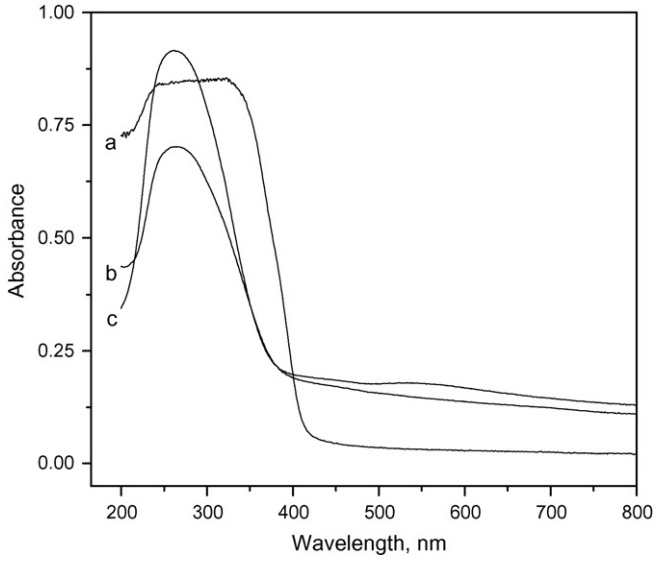

Fig. 6. Diffuse-reflectance UV–vis spectra of samples (b) T3 and (c) Au/T3. Curve (a) shows a comparative spectrum of E. Merck TiO_2 sample.

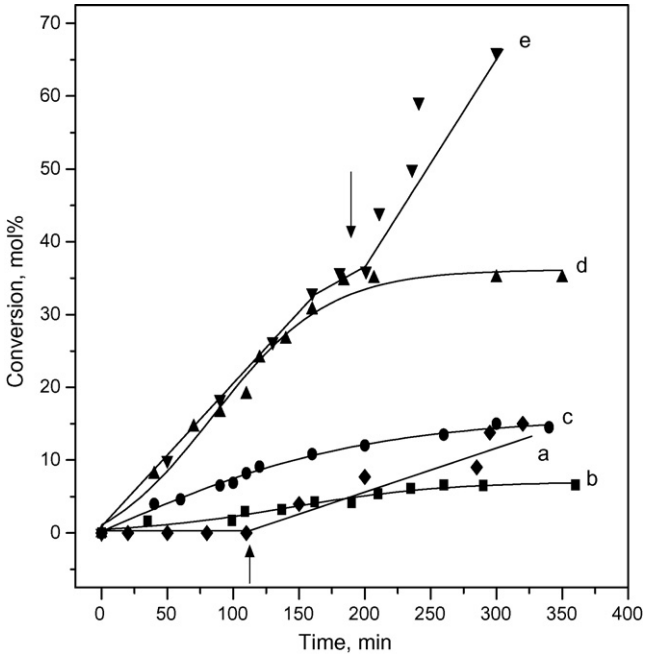

Fig. 7. Yield of CO_2 as a function of radiation dose when air mixed with different mole percent of benzene vapor reacted over Au (1%)/T3 catalyst under UV-irradiation. Curve (b) 2.3, (c) 1.5, (d) 0.78, and (e) 0.74 mol%. Curve (a) presents similar data for gold-free sample T3. The arrow shown on curves (a) and (e) indicate the change of reaction rate on addition of 150 μmol of water in the reaction cell.

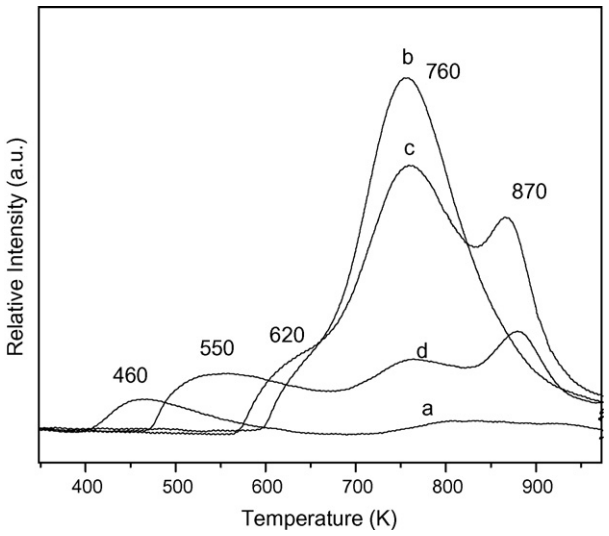

Fig. 8. Temperature-programmed desorption of saturation-covered O_2 from: (a) commercial (Merck) TiO_2, (b) mesoporous TiO_2 (sample T1), (c) TiO_2 nanotubes (sample T3) and (d) Au (1 wt%)/T3.

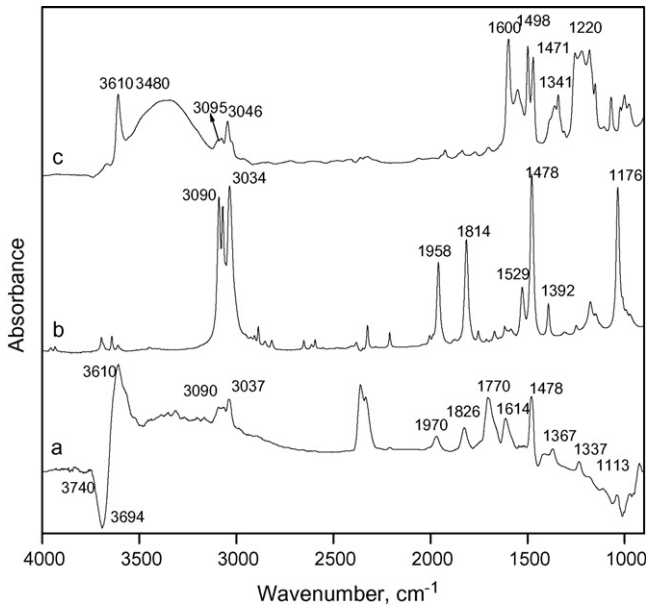

Fig. 9. Difference IR spectrum (DRIFT) of TiO_2 nanotubes (sample T3) exposed to benzene vapor (10 mol%) + air at room temperature (curve (a)). Curves (b) and (c), respectively show the IR spectra of liquid benzene and phenol in CCl_4.

Overall, our TPD results reveal that the presence of gold gives rise to certain new adsorption sites at Au-TiO_2 interfaces for the adsorption and activation of O_2 molecules. These O_2 molecules may in turn assist the photo-oxidation process (Fig. 7) by way of certain oxygen ion radicals generated on interaction with e^-/h^+ pair, as described below.

3.7. Infrared spectroscopy of surface adsorbed species

The uncompensated diffuse-reflectance infrared (DRIFT) spectrum of air-exposed nanotube sample T3 (not shown), flushed in nitrogen and with no benzene exposure, showed a broad band at 948 cm^{-1} representing the lattice vibrations of titanium dioxide, in addition to well-reported absorption bands in 3800–3000 cm^{-1} region and at 1635 cm^{-1} due to the O–H stretching and deformation vibrations of surface hydroxyl or adsorbed water molecules [22].

Curve (a) in Fig. 9 exhibits the spectrum of sample T3, recorded after exposure at room temperature to benzene vapor + air and plotted after compensating for the vibrational bands of an unexposed wafer. This spectrum reveals the removal of ν(OH) IR bands at 3740 and 3694 cm^{-1} (negative IR bands), indicating the active participation of water molecules and the surface hydroxyl groups during interaction of benzene molecules with TiO_2. To identify the vibrational bands in 3600–1000 cm^{-1} region in Fig. 9a, the IR spectra of liquid benzene and phenol (~1 mol% solution in CCl_4) are shown in curves (b) and (c), respectively, of Fig. 9. We observe that the spectrum in Fig. 9a does not match completely with either of the two spectra in curves (b) and (c). Also, the spectrum in Fig. 9a finds no match with the IR spectra of other possible benzene derivatives, such as hydroquinone and catechol. Comparing with the spectrum in Fig. 9b, the IR band at 1478 cm^{-1} (in-plane C–C stretching, ν_{19}), combination 3037 cm^{-1} band (C–C stretching, ν_{19} + C–C stretching, ν_8) and a band at 3090 cm^{-1} (C–H stretching, ν_{20}) may be identified with the corresponding vibrations of liquid benzene [23]. The relative intensity of these bands is, however, quite different. For instance, the intensity ratio of 1478 and 3037 cm^{-1} band is around 1 in Fig. 9b as compared to the value of ~2.5 in Fig. 9a. We also observe a considerable shift in the frequency of the out-of-plane benzene vibrations in the adsorbed species. Thus, the vibrational bands at 1814 cm^{-1} [C–H⊥ bending, ν_{17} + C–H⊥ bending, ν_{10}] and 1958 cm^{-1} [C–H⊥ bending, ν_{17} + C–H⊥ bending, ν_5] in Fig. 9b are found to shift to a higher frequency by ~12 cm^{-1} in Fig. 9a. Again, the intensity of these bands decreases considerably in the adsorbed state in comparison with the ν_{19} band at 1478 cm^{-1}. In addition to these features, we also observe a complete absence of several other benzene vibrations in Fig. 9a. For instance, no out-of-plane IR bands at 1529 cm^{-1} (ν_{11} + ν_{10}) and 1392 cm^{-1} (ν_{16} + ν_5) are seen in Fig. 9a in addition to several other weak bands (cf. Fig. 9b). The selective changes in the frequency and the intensity of the out-of-plane vibration of benzene has been attributed in earlier studies to the interaction of surface Ti^{4+} ions with the benzene ring through their π-system [8,24]. Indeed, an electronic interaction of benzene molecules at Ti^{4+} sites would lead to the lowering of their D_{6h} symmetry and hence in the changes in the vibrational modes. The lowering of the symmetry is known to result in the frequency shifts and band splitting.

In addition to the benzene bands mentioned above, we observe a prominent band at 3610 cm^{-1} in Fig. 9a, which corresponds closely with the ν(OH) band of phenol in Fig. 9c. The sharpness of this band is a characteristic feature of a gas phase or a very dilute solution of phenol [25], and is therefore indicative of the adsorbed state of phenol molecules over titania surface. The ν(CH) bands of phenol in 3100–3000 cm^{-1} region (Fig. 9c) overlap with the benzene bands in this region (Fig. 9a). As reviewed in [26], the IR spectra of phenols are characterized by the strong coupling of C–O stretching (νCO) and in-plane O–H bending (δOH) vibrations with the aromatic C–C and C–H movements, giving rise to sharp IR bands in the 1600–1000 cm^{-1} region. A number of sharp bands seen in Fig. 9a in this region may therefore be assigned to the isolated phenol molecules in their adsorbed state. The difference in the frequency and the intensity of these bands, compared to the corresponding IR bands in Fig. 9c, may thus be attributed to the perturbation of the phenol molecules because of their binding at the titania surface, as is also observed in an earlier study [8].

The IR bands of adsorbed benzene were removed completely on post exposure flushing of the sample in nitrogen but the phenolic bands were comparatively more stable. Flushing of the sample also revealed the presence of some new bands. Curves (a) and (b) in Fig. 10 show the comparative IR bands on sample T3 in 2000–

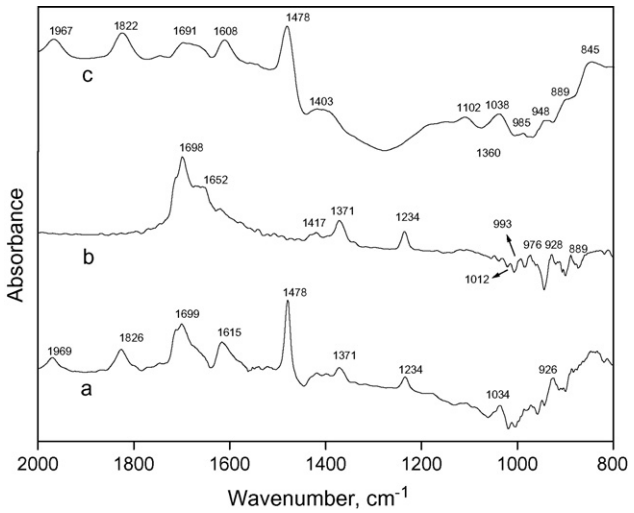

Fig. 10. Comparative DRIFT spectra in 2000–800 cm^{-1} region for T3 sample exposed to benzene + air (curve (a)) followed by 10 min flushing in nitrogen (curve (b)). Curve (c) shows IR spectrum of Au/T3 after exposure to benzene + air.

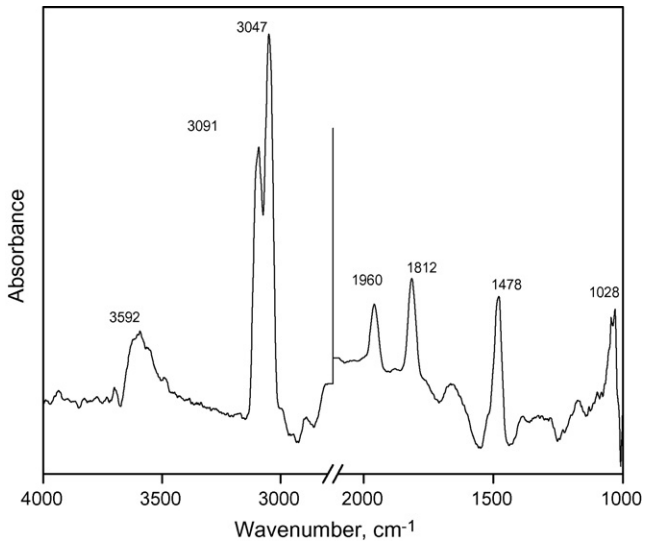

Fig. 11. Transmission mode IR spectrum of TiO_2 nanotubes (T3), dehydrated by heating at 600 K for 6 h under vacuum, followed by exposure to benzene + air at room temperature.

800 cm^{-1} region after exposure to benzene + air (curve (a)) and subsequent flushing for ~10 min (curve (b)). The set of vibrational bands seen in Fig. 10b do not match with the spectra of any of the viable phenol derivatives and may be tentatively ascribed to certain unidentified polymeric species, as reported in earlier studies [1,6]. The spectral features similar to those described above were observed in the experiments conducted over gold dispersed titania (Au/T3) sample as well. For instance, Fig. 10c presents the typical vibrational bands of Au/T3 after adsorption of benzene vapor + air, recorded under similar conditions. These results indicate that the surface species formed after benzene adsorption over titania remain unaffected by the presence of gold particles.

The presence of moisture in the sample was, however, found to play an important role. To probe the role of water, some transmission mode experiments were conducted where the sample was dehydrated completely by heating at 600 K for 6 h under vacuum prior to benzene adsorption. Fig. 11 presents a typical transmittance IR spectrum of a pre-activated sample T3, exposed to benzene + air at room temperature and recorded after compensating for the vibrational bands of clean titania sample. It is of interest to note that no IR bands due to phenol or any other reaction products are seen in Fig. 11. At the same time, IR bands of adsorbed benzene in this figure match well with the spectrum of liquid benzene (Fig. 9b), with no frequency shift or changes in the relative intensities (cf. Fig. 9a).

The IR results presented above thus clearly show that the water molecules adsorbed in TiO_2 play an important role, both in the binding of benzene molecules at titania surface and their subsequent transformation to phenolic species. This is contrary to the findings of Doucet et al. [11], where relative humidity is found to play no important role in the primary attack of benzene molecules over titania surface. At the same time, the formation of hydroxyl ($OH^{\bullet}$) and other oxygen-containing radicals at the surface of illuminated TiO_2 in presence of adsorbed water is a well-reported phenomenon; and the role of these species as primary oxidants in the photocatalytic processes has been highlighted in many articles [27,28]. Taking our activity results into consideration, where water addition is found to enhance the benzene conversion (Fig. 7), it is envisaged that the phenolic species may serve as important intermediates in photo-oxidation of benzene to form CO_2. The oxidation of phenols via formation of transient phenoxyl radicals ($ArO^{\bullet}$) or phenolate ions (ArO^{-}) is known to take place in a large variety of photochemical, thermochemical and radiation chemical processes [26]. Various possible pathways involving the metal ions, free radicals and inter-molecular electron transfer have been proposed in this context, as is reviewed in a recent article [26]. Some of the possible routes leading to the formation of phenol, phenolic group, phenoxyl radical or phenolate ions over TiO_2 surface without or in the presence of radiation may thus be represented as following.

4. Conclusion

In conclusion, the results of our study reveal two independent roles played by surface hydroxyl groups of titania and the dispersed particles of the gold co-catalyst. The hydroxyl groups and the adsorbed water molecules assist in the transformation of benzene molecules to surface adsorbed phenol or phenolic groups. It is envisaged that these species may convert to the phenoxyl radicals or phenolate ions in the presence of light and oxygen, as per the reaction mechanism shown above. It is imperative that large surface area and porous character of titania nanotubes would provide enhanced number of such reaction sites. In regards to the role of gold co-catalyst, several theories have been proposed. In general, it is believed that a noble metal (e.g. Pt, Au) acts as a sink for photo-induced charge carriers and promotes the interfacial charge transfer processes in the metal–TiO_2 composite systems [29]. A direct correlation has been demonstrated between the photo-electrochemical performances of semiconductor–metal films and the shift in the quasi-Fermi level of the composite to more negative potentials. As evident from our TPD-O_2 results [Fig. 8], in addition to the above mentioned roles, the nano-structured gold crystallites and Au/TiO_2 interfaces may also serve as independent sites for the adsorption and activation of oxygen molecules. The oxygen adsorbed at Au sites of the photo-excited Au/TiO_2 could act as an electron scavenger by forming O_2^{-} species. These ionic species as well as the hydroxyl radicals formed by oxidation of H_2O on photo-activated catalyst would in turn felicitate the deep oxidation of transient surface species shown in Scheme 1.

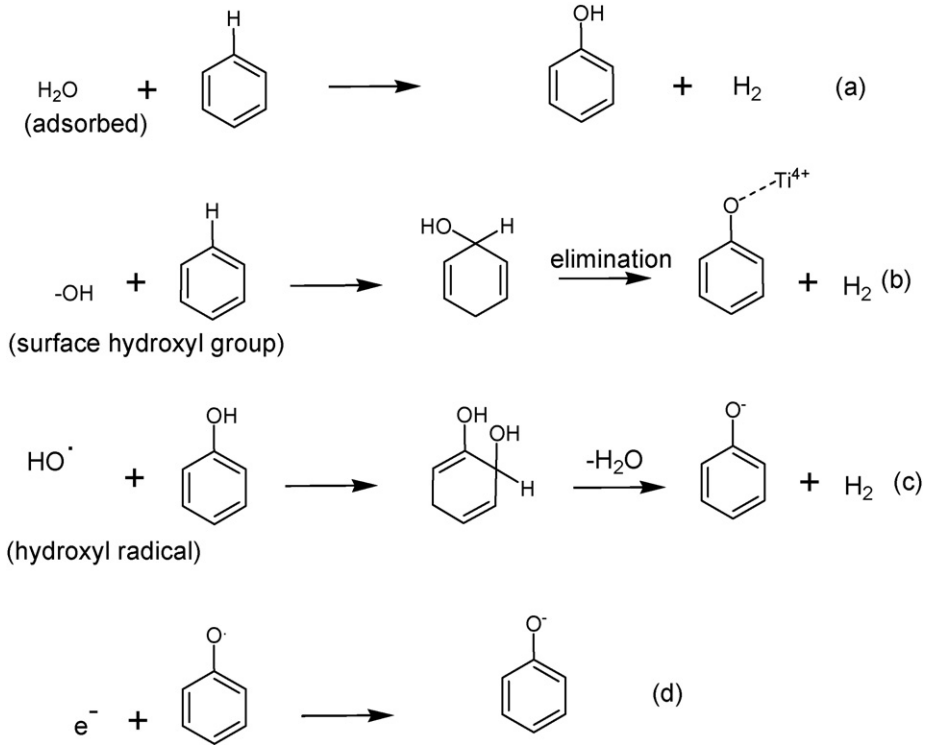

Scheme 1. Formation of phenol (a), phenolic group (b), phenoxyl radical (c) and phenolate ion (d) adsorbed over TiO_2 without (a and b) and in presence of radiation (c and d).

Acknowledgements

NMG thanks the Council of Scientific and Industrial Research (CSIR) Delhi, for a research grant under the Emeritus Scientist scheme.

References

[1] X. Fu, W.A. Zeltner, M.A. Anderson, Appl. Catal. B: Environ. 6 (1995) 209.
[2] H. Park, W. Choi, Catal. Today 101 (2005) 291.
[3] S.A. Larson, J.L. Falconer, Catal. Lett. 44 (1997) 57.
[4] H. Einaga, S. Futamura, T. Ibusuki, Phys. Chem. Chem. Phys. 1 (1999) 4903.
[5] K.-I. Shimizu, H. Akahane, T. Kodama, Y. Kitayama, Appl. Catal. A: Gen. 269 (2004) 75.
[6] J. Chen, L. Eberlein, C.H. Langford, J. Photochem. Photobiol. A: Chem. 148 (2002) 183.
[7] H. Einaga, S. Futamura, T. Ibusuki, Chem. Lett. (2001) 582.
[8] W.-C. Wu, L.-F. Liao, C.-F. Lien, J.-L. Lin, Phys. Chem. Chem. Phys. 3 (2001) 4456.
[9] N.N. Lichtin, M. Sadeghi, J. Photochem. Photobiol. A: Chem. 113 (1998) 81.
[10] O.D. Hennezel, P. Pichat, D.F. Ollis, J. Photochem. Photobiol. A: Chem. 118 (1998) 197.
[11] N. Doucet, O. Zahraa, M. Bouchy, Catal. Today 122 (2007) 168.
[12] G.-M. Zuo, Z.-X. Cheng, H. Chen, G.-W. Li, T. Miao, J. Hazard. Mater. B 128 (2006) 158.
[13] W. Wang, Y. Ku, J. Photochem. Photobiol. 159 (2003) 47.
[14] S.V. Awate, A.A. Belhekar, S.V. Bhagwat, R. Kumar, N.M. Gupta, Int. J. Photoenergy 2008 (2008) 13, Article ID 789149.
[15] R. Yoshida, Y. Suzuki, S. Yoshikawa, Mater. Chem. Phys. 91 (2005) 409.
[16] Y.Q. Wang, G.Q. Hu, X.F. Duan, H.L. Sun, Q.K. Xue, Chem. Phys. Lett. 365 (2002) 427.
[17] D.-S. Seo, J.-K. Lee, H. Kim, J. Cryst. Growth 229 (2001) 428.
[18] G.H. Du, Q. Chen, R.C. Che, Z.Y. Yuan, L.-M. Peng, Appl. Phys. Lett. 79 (2001) 3702.
[19] N.M. Gupta, in: B. Viswanathan, S. Sivasankar, A.V. Ramaswamy (Eds.), Catalysis Principles and Applications, Narosa, Delhi, 2001, p. 127.
[20] C.-M. Yang, M. Kalwei, F. Schuth, K.J. Chao, Appl. Catal. A: Gen. 254 (2003) 289.
[21] Y.-D. Wang, C.-L. Ma, X.-D. Sun, H.-D. Li, J. Non-Cryst. Solids 319 (2003) 109.
[22] G. Busca, H. Saussey, O. Saur, J.C. Lavalley, V. Lorenzelli, Appl. Catal. 14 (1985) 245.
[23] C.L. Angell, M.V. Howell, J. Colloids Interface Sci. 28 (1968) 279.
[24] Y. Suda, Langmuir 4 (1988) 147.
[25] S. Steenken, P. Neta, The chemistry of Phenols, Patai Series: The chemistry of Functional Groups, Part I, Ed- Zvi Rappoport, Wiley, England, 2003, p. 370.
[26] S. Steenken, P. Neta, The Chemistry of Phenols, Patai Series: The chemistry of Functional Groups, Part II, Ed- Zvi Rappoport, Wiley, England, 2003, p. 1107.
[27] C.S. Turchi, D.F. Ollis, J. Catal. 122 (1990) 178.
[28] Z. Yu, S.S.C. Chuang, J. Catal. 246 (2007) 118.
[29] V. Subramanian, E. Wolf, P.V. Kamath, J. Phys. Chem. B 105 (2001) 11439.